Featured in Physics

Driving Alkali Rydberg Transitions with a Phase-Modulated Optical Lattice

R. Cardman* and G. Raithel
Department of Physics, University of Michigan, Ann Arbor, Michigan 48109, USA

(Received 9 October 2022; accepted 23 May 2023; published 11 July 2023)

We develop and demonstrate a spectroscopic method for Rydberg-Rydberg transitions using a phase-controlled and -modulated, standing-wave laser field focused on a cloud of cold ^{85}Rb Rydberg atoms. The method is based on the ponderomotive ($\boldsymbol{A}^2$) interaction of the Rydberg electron, which has less-restrictive selection rules than electric-dipole couplings, allowing us to probe both $nS_{1/2} \rightarrow nP_{1/2}$ and $nS_{1/2} \rightarrow (n+1)S_{1/2}$ transitions in first order. Without increase in laser power, third- and fourth-order subharmonic drives are employed to access Rydberg transitions in the 40 to 70 GHz frequency range using widely available optical phase modulators in the Ku band (12 to 18 GHz). Measurements agree well with simulations based on the model we develop. The spectra have prominent Doppler-free components with linewidths $\lesssim$200 kHz. The method paves the way for optical Doppler-free high-precision spectroscopy of Rydberg-Rydberg transitions and for spatially selective qubit manipulation with μm-scale resolution in Rydberg-based simulators and quantum computers, provided that magic states are chosen and that the atoms are sufficiently cold.

DOI: 10.1103/PhysRevLett.131.023201

Innovations in quantum technologies based on Rydberg atoms rely on manipulation of their internal states. Technologies include simulators exploring quantum phase transitions and walks [1–5], quantum processors [6,7], and Rydberg-atom-based sensors [8,9]. It is often beneficial to trap and arrange the Rydberg atoms using tightly focused laser beams, optical-tweezer arrays, or optical lattices to configure such systems. Coherent interactions on Rydberg qubits can be performed with rf to sub-THz radiation. The diffraction limit of $\gtrsim$1 mm then potentially disallows single-qubit operations or short-distance gates. One method to achieve spatial selectivity of Rydberg transitions on a μm scale, required in many of these applications, is through optical addressing of isolated-core excitations (ICE) in alkaline-earth atoms [10–16], but limitations of the ICE method include autoionization of low-l Rydberg states due to Rydberg-ICE interaction. Also, ICE addressing is not practical in commonly used alkali atomic species. Here, we explore direct optical drives of Rydberg transitions as a more widely applicable method with μm-scale spatial selectivity.

Rydberg transitions can be directly optically driven through ponderomotive interactions, $e^2A^2/2m_e$, where $\boldsymbol{A}$ is the vector potential of the driving laser [17]. Driving ponderomotive transitions entails generating an optical intensity gradient that is spatially varying within the Rydberg electron's wave function, and modulating the intensity distribution at (a subharmonic of) the atomic transition frequency. Suitable control of the modulation frequency leads to transitions between Rydberg states. Ponderomotive transitions in modulated optical lattices typically have a Doppler-free component with an interaction-time-limited linewidth [18]. Ponderomotive Rydberg atom spectroscopy has been previously performed by amplitude-modulating an optical lattice, allowing transitions between states $\{|0\rangle, |1\rangle\}$ of equal parity, i.e., $\langle 0|\hat{\Pi}|0\rangle = \langle 1|\hat{\Pi}|1\rangle$ [17]. Odd-parity ($\langle 0|\hat{\Pi}|0\rangle = -\langle 1|\hat{\Pi}|1\rangle$) transitions are forbidden for this drive method, unless the modulation is detuned from resonance by the lattice trap-oscillation frequency [18,19] and the atom's motional quantum state ν is changed, which is generally undesirable. On the other hand, Rydberg quantum simulators operating on electric-dipole interactions between atoms sometimes require the preparation of a mixed-parity system (e.g., nS and $n'P$ atoms [3,5,20]). Harnessing optically driven ponderomotive transitions for Rydberg quantum simulators therefore requires a generalization that will allow local odd-parity transitions without motional excitation of the atoms.

In this Letter, we demonstrate optically driven alkali Rydberg transitions using an optical lattice that is phased-modulated at a subharmonic $\omega_m = \omega_0/q$ of the atomic transition frequency ω_0, with an integer subharmonic order q. The transitions occur in first-order perturbation theory even at large q, no intermediate atomic states are involved, and the required optical-field strengths do not increase with q (see Appendix A). Optical setup, selection rules, and transition Rabi frequencies in phase-modulated lattices fundamentally differ from the case of amplitude modulation. Phase modulation of the laser allows both odd- and even-parity transitions without change of the motional number ν. Here, we perform ponderomotive optical spectroscopy of ^{85}Rb transitions by scanning the lattice

phase-modulation frequency ω_m over a subharmonic of the atomic resonance, $\omega_m \approx \omega_0/q$. A one-dimensional lattice with counterpropagating laser beams is used (wavelength $\lambda = 2\pi c/\omega_L = 2\pi/k_L = 1064$ nm), and, in a single setup, both odd-parity $nS_{1/2} \to nP_{1/2}$ ($\langle 0|\hat{\Pi}|0\rangle = -\langle 1|\hat{\Pi}|1\rangle$) and even-parity $nS_{1/2} \to (n+1)S_{1/2}$ ($\langle 0|\hat{\Pi}|0\rangle = \langle 1|\hat{\Pi}|1\rangle$) spectra are studied.

The lattice is constituted of three colinear beams, a pair of left(r)- and right(i)-propagating unmodulated beams with optical fields $\boldsymbol{E}_u^{(i)}$ and $\boldsymbol{E}_u^{(r)}$, plus a beam with field $\boldsymbol{E}_m^{(i)}$ that is phase-modulated at ω_m and coaligned with $\boldsymbol{E}_u^{(i)}$. The constant phase difference between the modulated and unmodulated beams is denoted η_0, and the amplitude of the phase modulation η_1. A phase $\eta_2(t)$ is optionally applied to translate the lattice along the atom's center-of-mass coordinate, Z_0. Equation (A1) of the Appendix A gives expressions for these fields.

The ponderomotive interaction is given by the mean square of the field in Eq. (A1) (Appendix A), averaged in time over many optical cycles and a small fraction of $2\pi/\omega_m$. One finds a time-independent component that constitutes a positive optical-lattice atom-trapping potential with an offset, $U_0 \cos[2k_L Z_0 + \eta_2(t)] + U_{\rm ofs}$, and a time-dependent atom-field interaction potential, $U_{\rm AF}(Z_0, t)$, that couples states $|0\rangle$ and $|1\rangle$. For the latter we find

$$U_{\rm AF}(Z_0, t) = \frac{\hbar}{2}\Omega_{q,0}|\cos(2k_L Z_0)|e^{i(\xi - q\omega_m t)}|1\rangle\langle 0| + \text{H.c.}, \tag{1}$$

where $\Omega_{q,0}|\cos(2k_L Z_0)|$ is the Z_0-dependent Rabi-frequency magnitude for the qth subharmonic drive, and ξ is the Z_0-dependent phase of the atom-field coupling. Coupling strength, $|U_{\rm AF}|$, and phase, $\xi(Z_0)$, are plotted in Fig. 1. Owing to the staircase shape of $\xi(Z_0)$, which is inherent to ponderomotive lattice-modulation spectroscopy, the method represents a paradigm of Doppler-free spectroscopy.

In our first demonstration of lattice phase-modulation drive, we prepare ^{85}Rb atoms in $|0\rangle = |46S_{1/2}\rangle$ from a sample of ground-state atoms laser-cooled and localized near local maxima of the 1064-nm lattice intensity using off-resonant ($\Delta = +140$ MHz), two-photon laser excitation with 780- and 480-nm light. It is $\eta_0 = \eta_2 = 0$, while η_1 is pulsed on from zero to $1.3(3)\pi$ for the duration of the drive, $\tau = 6$ μs. We measure the $|0\rangle \to |1\rangle = |46P_{1/2}\rangle$ transition, which has a lattice-free transition frequency $\omega_0/2\pi = 39.121\,294$ GHz. We use a subharmonic order $q = 3$, and the modulation frequency $\omega_m/2\pi$ is scanned from 13.040 211 GHz to 13.040 633 GHz in steps of 3 kHz. Notably, the $q = 3$ subharmonic drive allows us to project the Rydberg transition (frequency ∼39 GHz) into the Ku band (12–18 GHz), for which efficient optical fiber modulators exist. Internal-state populations of $|0\rangle$ and $|1\rangle$ are counted with state-selective field ionization [21] (Appendix B). Figure 2 shows the spectrum with an overlapped numerical simulation (for details of the simulation, see Supplemental Material [22]).

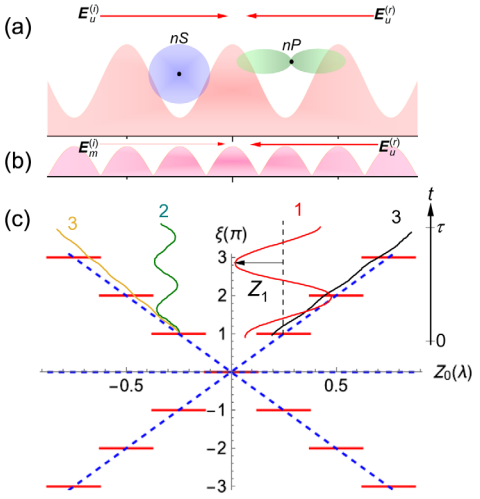

FIG. 1. (a) Qualitative sketch of the trapping potential, $U_0 \cos[2k_L Z_0 + \eta_2(t)] + U_{\rm ofs}$, created by $\boldsymbol{E}_u^{(i)}$ and $\boldsymbol{E}_u^{(r)}$, vs center-of-mass position Z_0, with two Rydberg atoms roughly to scale. (b) Qualitative magnitude of the atom-field drive, $|U_{\rm AF}|(Z_0)$, formed by $\boldsymbol{E}_m^{(i)}$ and $\boldsymbol{E}_u^{(r)}$. (c) Phase of the atom-field drive, $\xi(Z_0)$ (red solid), in comparison with phase functions that would apply to Raman transitions (blue dashed). Several trapped (1, 2) and untrapped (3) atom trajectories vs time, $Z_0(t)$, are plotted on top (details, see text).

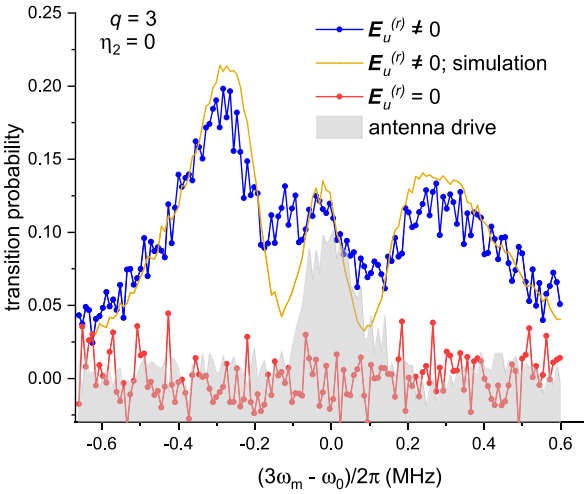

FIG. 2. Population in $|1\rangle$ as ω_m is scanned over $\omega_0/3$ in 3 kHz steps. Here, $|0\rangle = |46S_{1/2}\rangle$ and $|1\rangle = |46P_{1/2}\rangle$. The blue signal is an average of 10 individual ω_m scans with 400 measurements each and $\boldsymbol{E}_u^{(r)}$ unblocked. The gold line is a corresponding numerical simulation. The pink signal shows the population in $|1\rangle$ when $\boldsymbol{E}_u^{(r)}$ is blocked for an average of 4 individual scans with 400 measurements each. The shaded spectrum shows a single-photon microwave drive using a horn antenna without any 1064-nm light. In all spectra, $\tau = 6$ μs.

The peak Rabi frequency $\Omega_{q=3,0}$ in Eq. (1) for the case of Fig. 2 has the following dependence on experimental parameters:

$$\Omega_{q=3,0} = -\frac{\alpha_e(\omega_L)}{\hbar}\mathcal{E}_m^{(i)}\mathcal{E}_u^{(r)}(\hat{\epsilon}^{(i)}\cdot\hat{\epsilon}^{(r)}) \times \langle 1|\sin(2k_L z_e)|0\rangle J_3(\eta_1), \quad (2)$$

where $\alpha_e(\omega_L)$ is the free-electron polarizability for light at angular frequency ω_L and z_e the electronic coordinate. This quantity is -545 a.u. for 1064 nm. For the spectrum in Fig. 2, we estimate $\Omega_{3,0} \sim 2\pi \times 70$ kHz and $U_0 \sim h \times 2.5$ MHz by comparing simulated and experimental signals. When $\boldsymbol{E}_u^{(r)}$ is extinguished, the Rabi frequency vanishes, as the intensity gradient in the laser field no longer varies within the Rydberg-electron wave function. This test proves that there is no population transfer into $|1\rangle$ by means of higher-order $\boldsymbol{A}\cdot\boldsymbol{p}$ interactions originating from microwave leakage, and that the observed transfer into $|1\rangle$ is entirely due to the $\boldsymbol{A}^2$ interaction in the modulated optical lattice.

Three peaks appear in the spectrum in Fig. 2. The central peak is free of Doppler shifts, conserves the motional state ν, and has a linewidth of ~200 kHz (measured with a peak fit). This peak arises from trapped atoms with large oscillation amplitudes Z_1 (trajectory 1 in Fig. 1). The phases ξ near the turning points, where the oscillating atom spends most of its time, differ by 2π, leading to a predominantly fixed-phase Doppler-free drive. The broad sidebands at about ± 300 kHz correspond to Doppler shifts of atoms traveling over many lattice wells (trajectories 3 in Fig. 1). Those atoms move across multiple steps of $\xi(Z_0)$ at a roughly constant velocity v along z, and exhibit a Doppler shift according to the time average

$$\langle\dot{\xi}\rangle \simeq \frac{d\xi}{dZ_0}\langle v\rangle \simeq \frac{4\pi}{\lambda}\langle v\rangle = 2k_L\langle v\rangle. \quad (3)$$

There, we use the fact that the average slope of the step functions in Fig. 1 is $d\xi/dZ_0 \simeq 4\pi/\lambda$. Additionally, the sidebands contain signals from trapped atoms undergoing motional-state changes of $\Delta\nu = \pm 2$, causing an asymmetry in the transition strengths [18]. Both physical origins of the sidebands are different and do not interfere.

The strength of the sidebands in Fig. 2 relative to the Doppler-free line follows from the Rydberg excitation scheme. Rb $|5S_{1/2}\rangle$ atoms, which have a positive ac polarizability, are laser-cooled and trapped at the lattice-intensity maxima. Rydberg excitation lasers are tuned to the ground-Rydberg resonance at the lattice-intensity maxima. Because the ponderomotive force generally repels Rydberg atoms from regions of high laser intensity, most Rydberg atoms prepared in this way are not trapped along z and traverse over multiple lattice periods during the atom-field interaction, partially giving rise to the strong sidebands in Fig. 2. A minority of the Rydberg atoms is barely trapped in the Rydberg-atom lattice (trajectory 1 in Fig. 1), which suffices to produce the observed Doppler-free peak. The vibrational wave functions of the barely trapped atoms peak close to lattice-intensity maxima, where the differential light shift between states $|0\rangle$ and $|1\rangle$ is negative, causing a redshift of the Doppler-free peak relative to the field-free atomic resonance [23,27]. Large oscillation amplitudes Z_1 also are conducive to changes in the motional quantum number ν of trapped atoms by ± 2, causing extra signal within the locations of the sidebands [18].

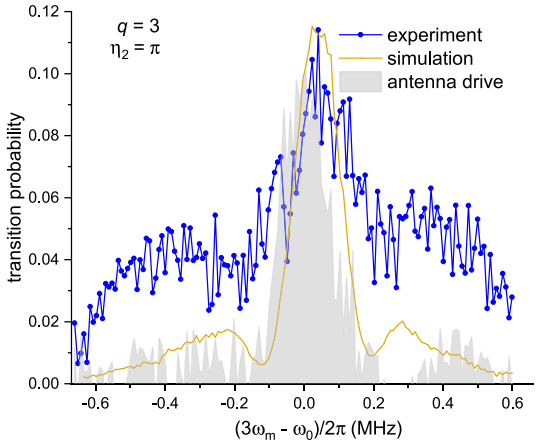

FIG. 3. Spectrum measured for the same states and same conditions as in Fig. 2, except that the lattice is suddenly shifted in position by $\lambda/4$ between Rydberg-atom preparation and modulated-lattice drive.

To enhance the visibility of the Doppler-free peak relative to the sidebands, we suddenly shift the optical lattice in z by $\lambda/4$ immediately after Rydberg-atom preparation. The shift, implemented by a phase step function $\eta_2(t)$ with step size π in Eq. (A1) (Appendix A), places the atoms near a lattice-intensity minimum during atom-field interaction [23]. Most atoms are then trapped while being probed, and the Doppler-free peak becomes larger than the side peaks. Since $Z_1 \lesssim 0.125\lambda$ in this case, ξ is fixed throughout the interaction time (trajectory 2 of Fig. 1), also leading to a Doppler-free drive. In Fig. 3 we show a spectrum for the same transition as in Fig. 2, with the $\lambda/4$ lattice translation applied. The Doppler-free peak in Fig. 3 increases in strength relative to Fig. 2, as expected, and in Fig. 3 it is blueshifted due to a positive differential light shift between states $|0\rangle$ and $|1\rangle$ near the lattice-intensity minima [23,27], providing evidence for a large proportion of atoms being collected and trapped near the intensity minima.

While the sidebands in Fig. 3 are suppressed, as expected, they are stronger in the measurement than in the simulation result. We attribute the disagreement to the fact that the lattice translation is not perfectly instantaneous, causing a dragging effect. Classically, Rydberg atoms that are initially excited near a maximum of the

Rydberg-atom trapping potential begin rolling down the potential during the not-quite-instantaneous translation, causing an increased fraction of nontrapped atoms. Also, the atoms that are successfully captured in the lattice wells experience center-of-mass heating due to the dragging.

In both Figs. 2 and 3 the central Doppler-free components are broader than in the antenna drive spectrum and in the simulations, where the FWHM of the Doppler-free components is near the Fourier limit of ≈150 kHz. This excess broadening of the experimental Doppler-free components likely arises from the $46P_{1/2}$ hyperfine structure [28], stray magnetic fields, and possible Rydberg dipole-dipole interactions. Also, state $|1\rangle$ experiences a shallower lattice depth than $|0\rangle$, yielding Z_0-dependent light shifts, $\Delta \propto \cos(2k_L Z_0)$. The resultant inhomogeneous broadening within the lattice wells primarily broadens the Doppler-free component and may cause it to overlap with the Doppler-shifted peaks. Lowering the temperature from our estimated 200 μK and eliminating the dragging in Fig. 3 would reduce the inhomogeneity and enhance the transition strength (see simulations in the Supplemental Material). Magic lattices, such as for $n = 69$ in our case, have $\Delta = 0$ for all Z_0 and are insensitive to inhomogeneous broadening within the wells, resulting in narrower and better-defined Doppler-free peaks (as calculated in [18]), making them a good choice for quantum-gate operations, where high fidelity is required. Finally, imperfections across the lattice, such as intensity variations and running-wave components, can cause additional differential shifts and inhomogeneous broadening.

Next, we demonstrate Doppler-free ponderomotive lattice phase-modulation spectroscopy for Rydberg states $|0\rangle$ and $|1\rangle$ of same parity, which are not subject to line broadening from electric-dipole interactions. We choose $|0\rangle = |48S_{1/2}\rangle$ and $|1\rangle = |49S_{1/2}\rangle$. The sample is initialized in $|0\rangle$, for which our lattice potential has a half-depth $U_0 = h \times 2.5$ MHz. The phases η_0 and η_2 are set to zero, the subharmonic order is $q = 4$, and $\omega_m/2\pi$ is scanned from 17.618 785 to 17.619 065 GHz in steps of 2 kHz. The modulation parameter η_1 is set to $1.7(4)\pi$ such that the $q = 4$ peak coupling in Eq. (1) becomes large ($\Omega_{4,0} \sim 2\pi \times 90$ kHz for our case). The interaction time between atoms and the phase-modulated lattice is $\tau = 12$ μs.

Figure 4 shows our results for the even-parity $|0\rangle \rightarrow |1\rangle$ spectrum. There are no transitions when blocking $\boldsymbol{E}_u^{(r)}$, which proves that the observed spectrum cannot be a high-order transition driven by stray microwave radiation, nor can it be an optical stimulated Raman transition driven by the remaining unidirectional, phase-modulated laser beam. A Lorentzian fit to the Doppler-free central peak has a FWHM linewidth of 96 kHz, which is in line with our Rabi-frequency estimate and the linewidth in the simulated spectrum. The small redshift of the lattice-driven Doppler-free peak relative to the microwave reference peak, which is a two-photon transition, reflects a differential light shift between states $|0\rangle$ and $|1\rangle$ at the standing-wave maxima.

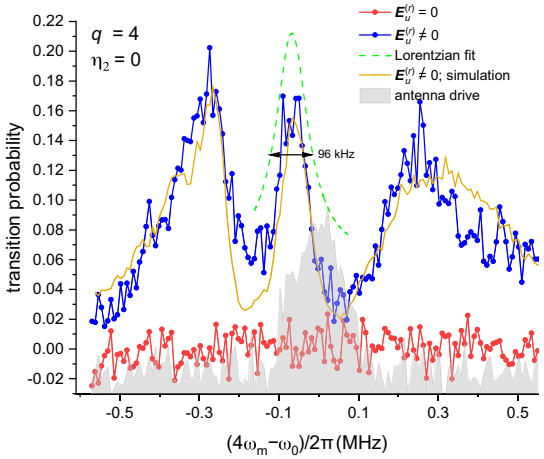

FIG. 4. Population in $|1\rangle$ as ω_m is scanned over $\omega_0/4$ in 2 kHz steps. In this spectrum, $|0\rangle = |48S_{1/2}\rangle$, $|1\rangle = |49S_{1/2}\rangle$, and $\omega_0/2\pi = 70.475\,710$ GHz. The blue signal is an average of 10 individual ω_m scans with 400 measurements each and $\boldsymbol{E}_u^{(r)}$ unblocked. The green, dashed line is a Lorentzian fit of the Doppler-free, $\Delta\nu = 0$ line, revealing a linewidth of 96 kHz. The gold line represents a numerical simulation result scaled down by 50%, accounting for an inefficiency in state-selective detection. The pink signal shows the population in $|1\rangle$ when $\boldsymbol{E}_u^{(r)}$ is blocked for an average of 6 individual scans with 400 measurements each. The shaded spectrum shows a two-photon microwave drive using a horn antenna for $\tau = 6$ μs without any 1064-nm light.

We finally discuss why Figs. 2–4 demonstrate a type of Doppler-free spectroscopy. Semiclassically, an atom moves on a trajectory $Z_0(t)$ as it is being probed. In spectroscopy based on the $\boldsymbol{A} \cdot \boldsymbol{p}$ interaction, the phase function usually is $\xi(Z_0) = \Delta k Z_0$, and the first-order Doppler effect is $\dot{\xi} = \Delta k v$. If atoms underwent a stimulated Raman transition (notably nonexistent, in our work) in counterpropagating lattice beams with wave numbers $\pm k_L$, there would be three branches of $\xi(Z_0)$, namely $\xi = 0$, corresponding to a Doppler-free spectral component, and $\xi = \pm 2k_L Z_0$, corresponding to spectral components with Doppler shifts $\pm 2k_L v$ [blue dashed lines in Fig. 1(c)]. Whereas, lattice-trapped atoms probed by ponderomotive lattice-modulation spectroscopy either remain on a single step of the staircase function [trajectory 2 in Fig. 1(c)] or predominantly reside on steps differing by 2π [trajectory 1 in Fig. 1(c)], resulting in Doppler-free excitation in either case, as in the Doppler-free component of a hypothetical Raman transition [horizontal blue dashed line in Fig. 1(c)]. Untrapped atoms (trajectories 3) run over many steps, resulting in approximately the same Doppler effect as in the Doppler-shifted Raman transitions [diagonal blue dashed lines in Fig. 1(c)]. The underlying $\mathbf{A}^2$-drive mechanism, the staircase shape of $\xi(Z_0)$, and off-resonant atom trapping in domains of fixed ξ

make ponderomotive lattice-modulation spectroscopy a novel type of Doppler-free spectroscopy.

In summary, we have observed both even- and odd-parity ponderomotive Rydberg transitions with linewidths $\lesssim$200 kHz using a phase-modulated optical lattice. We believe that subharmonic driving with the lattice is feasible for $q < 10$ (see Appendix A). Doppler- and recoil-free $|nS_{1/2}\rangle \rightarrow |n'P_{1/2}\rangle$ optically driven Rydberg transitions, demonstrated here, are useful for spin manipulations in quantum simulators [3,5], especially in protocols that require site-selective excitations. Doppler- and recoil-free $|nS_{1/2}\rangle \rightarrow |n'S_{1/2}\rangle$ transitions, also demonstrated here, are useful in high-precision spectroscopy where strong electric-dipole interactions between Rydberg atoms are to be avoided [29]. Far-reaching elimination of orbital-angular-momentum selection rules, which the technique described here provides, permits coherent preparation of Rydberg states with l as large as $n-1$ [30], as well as high-precision spectroscopy on such states in first order, applicable to determining constants that deepen our understanding of fundamental physics [29]. Optical couplings of Rydberg states free of the usual selection rules, afforded by ponderomotive lattice modulation spectroscopy, open access to higher-dimensional Hilbert spaces, including circular Rydberg states, allowing novel methods for quantum-state engineering and control [30–32]. Lattices in the synthetic dimension [20,33] of the Rydberg internal-state space can also be generated using the ponderomotive light-matter interaction presented here. Lastly, in alkaline-earth Rydberg atoms, the ponderomotive interaction, at suitable frequencies, would enable spatially selective addressing of the Rydberg electron, with the core electrons remaining spectators.

This work was supported by NSF Grant No. PHY-2110049. R. C. acknowledges support from the Rackham Predoctoral Fellowship.

Appendix A: Optical lattice field.—The laser fields forming the optical lattice are

$$\begin{aligned}
\boldsymbol{E}_u^{(i)}(\boldsymbol{R}_0+\boldsymbol{r}_e,t) &= \hat{\epsilon}^{(i)}\mathcal{E}_u^{(i)}(\boldsymbol{R}_0)\cos\left[k_L(Z_0+z_e)-\omega_L t+\eta_2(t)\right],\\
\boldsymbol{E}_u^{(r)}(\boldsymbol{R}_0+\boldsymbol{r}_e,t) &= \hat{\epsilon}^{(r)}\mathcal{E}_u^{(r)}(\boldsymbol{R}_0)\cos\left[k_L(Z_0+z_e)+\omega_L t\right],\\
\boldsymbol{E}_m^{(i)}(\boldsymbol{R}_0+\boldsymbol{r}_e,t) &= \hat{\epsilon}^{(i)}\mathcal{E}_m^{(i)}(\boldsymbol{R}_0)\cos\left[k_L(Z_0+z_e)-\omega_L t+\eta_0+\eta_1\cos\left(\omega_m\Delta s/c-\omega_m t\right)+\eta_2(t)\right],
\end{aligned} \tag{A1}$$

where $\boldsymbol{R}_0$ is the atom's center-of-mass vector, $\boldsymbol{r}_e$ is the Rydberg-electron vector operator, $\hat{\epsilon}^{(i)}, \hat{\epsilon}^{(r)}$ are polarization vectors of the right(i)- and left(r)-propagating beams, η_0 accounts for spurious phase offsets between modulated and unmodulated beams, η_1 is the modulation amplitude, and Δs is the path length of the modulated beam from the phase modulator to the atoms. The step-function phase jump $\eta_2(t)$ is optionally applied to both i beams immediately after laser excitation of the Rydberg atoms in the lattice. The phase jump, if applied, effects a sudden translation of the lattice relative to the atoms before the spectroscopic sequence. In our experiments, $\mathcal{E}_m^{(i)}$ (peak power of 12 mW) is about one-tenth the magnitudes of $\mathcal{E}_u^{(i)}$ (peak power of 880 mW) and $\mathcal{E}_u^{(r)}$ (peak power of 940 mW). The three beams are overlapped and focused down to a waist of $\sim$15 μm in the center of a ^{85}Rb optical molasses (see Supplemental Material for a detailed schematic of the optics). To form an optical lattice, the polarization vectors of all beams are kept linear and parallel with the optics shown in the Supplemental Material. Combined, the ponderomotive interaction, time-dependent at the order of the Rydberg electron's Kepler frequency, yields the atom-field interaction potential given in Eq. (1). Odd-parity transitions are driven for odd integer values of q and have $\Omega_{q,0} \propto \langle 1|\sin(2k_L z_e)|0\rangle$ while even-parity transitions are driven for even q and $\Omega_{q,0} \propto \langle 1|\cos(2k_L z_e)|0\rangle$. A complete derivation is provided in the Supplemental Material.

The subharmonic order q does not appear in the atomic matrix elements $\langle 1|\sin(2k_L z_e)|0\rangle$ and $\langle 1|\cos(2k_L z_e)|0\rangle$. For this reason, subharmonic ponderomotive lattice phase-modulation spectroscopy does not require substantial increases in laser intensity (if any) to drive transitions in increasing subharmonic order q. Hence, the frequency reduction afforded by the subharmonic drive does not come at the expense of larger ac shifts and lattice-induced photoionization rates. This benefit stands in contrast with multiphoton microwave spectroscopy, where both field intensity required and ac shifts increase drastically with q. From the Bessel function $J_q(\eta_1)$ in Eq. (2), it is apparent that subharmonic ponderomotive lattice phase-modulation spectroscopy comes with two minor penalties: (1) a higher microwave power for η_1 to reach the first extremum of $J_q(\eta_1)$ and (2) a mild drop-off of the atom-field coupling, which scales linearly in $J_q(\eta_1)$. For instance, an increase from $q=4$ (used in Fig. 4) to $q=10$ requires an increase in η_1 by about a factor of 2.2, corresponding to about a factor of 5 in microwave power supplied to the phase modulator, while the atom-field coupling drops by only about 40%. These minor penalties are heavily outweighed by the massive expansion of accessible Rydberg-transition frequency ranges afforded by high-order subharmonic drives. Practical factors presently limiting q to $q<10$ are phase sensitivities and rf damage thresholds of

commercially available phase modulators. In addition, for any target transition with a given subharmonic order $q < 10$, modulation frequency ω_m, and initial state, the chances that the same initial state has another transition at frequency $q'\omega_m$ with $q' \neq q$ and within a few tens of MHz from the target transition are very small. (It is straightforward to check for such coincidences.) In comparison, high-precision microwave spectroscopy of Rydberg transitions in 10th order would fundamentally not be feasible.

Appendix B: State-selective field ionization.—State-selective field ionization at a given modulation frequency yields a ratio of Rb ions that were in state $|1\rangle$ prior to ionization to all detected Rb ions by means of a gated particle counter (SRS Model SR400). The "transition probability" axes for all collected optical spectra in this Letter are these ratios subtracted by the average of all points in the spectrum where $\boldsymbol{E}_u^{(r)} = 0$ and no spectral feature is observed (pink data points in Figs. 2 and 4). We do this to eliminate any unwanted background signal from electrons and ions that were not involved in the spectroscopy but were recorded by the particle counter.

*Corresponding author.
rcardman@umich.edu

[1] H. Bernien, S. Schwartz, A. Keesling, H. Levine, A. Omran, H. Pichler, S. Choi, A. S. Zibrov, M. Endres, M. Greiner *et al.*, Nature (London) **551**, 579 (2017).
[2] T. L. Nguyen, J. M. Raimond, C. Sayrin, R. Cortiñas, T. Cantat-Moltrecht, F. Assemat, I. Dotsenko, S. Gleyzes, S. Haroche, G. Roux, T. Jolicoeur, and M. Brune, Phys. Rev. X **8**, 011032 (2018).
[3] A. Browaeys and T. Lahaye, Nat. Phys. **16**, 132 (2020).
[4] P. Scholl, M. Schuler, H. J. Williams, A. A. Eberharter, D. Barredo, K.-N. Schymik, V. Lienhard, L.-P. Henry, T. C. Lang, T. Lahaye *et al.*, Nature (London) **595**, 233 (2021).
[5] M. Khazali, Quantum **6**, 664 (2022).
[6] M. Saffman, T. G. Walker, and K. Mølmer, Rev. Mod. Phys. **82**, 2313 (2010).
[7] S. R. Cohen and J. D. Thompson, PRX Quantum **2**, 030322 (2021).
[8] C. L. Holloway, J. A. Gordon, S. Jefferts, A. Schwarzkopf, D. A. Anderson, S. A. Miller, N. Thaicharoen, and G. Raithel, IEEE Trans. Antennas Propag. **62**, 6169 (2014).
[9] D. H. Meyer, Z. A. Castillo, K. C. Cox, and P. D. Kunz, J. Phys. B **53**, 034001 (2020).
[10] R. M. Jopson, R. R. Freeman, W. E. Cooke, and J. Bokor, Phys. Rev. Lett. **51**, 1640 (1983).
[11] R. R. Jones and T. F. Gallagher, Phys. Rev. A **38**, 2846 (1988).
[12] R. R. Jones, C. J. Dai, and T. F. Gallagher, Phys. Rev. A **41**, 316 (1990).
[13] H. Lehec, X. Hua, P. Pillet, and P. Cheinet, Phys. Rev. A **103**, 022806 (2021).
[14] A. Muni, L. Lachaud, A. Couto, M. Poirier, R. C. Teixeira, J.-M. Raimond, M. Brune, and S. Gleyzes, Nat. Phys. **18**, 502 (2022).
[15] K.-L. Pham, T. F. Gallagher, P. Pillet, S. Lepoutre, and P. Cheinet, PRX Quantum **3**, 020327 (2022).
[16] A. P. Burgers, S. Ma, S. Saskin, J. Wilson, M. A. Alarcón, C. H. Greene, and J. D. Thompson, PRX Quantum **3**, 020326 (2022).
[17] K. R. Moore, S. E. Anderson, and G. Raithel, Nat. Commun. **6**, 6090 (2015).
[18] V. S. Malinovsky, K. R. Moore, and G. Raithel, Phys. Rev. A **101**, 033414 (2020).
[19] B. Knuffman and G. Raithel, Phys. Rev. A **75**, 053401 (2007).
[20] S. Kanungo, J. Whalen, Y. Lu, M. Yuan, S. Dasgupta, F. Dunning, K. Hazzard, and T. Killian, Nat. Commun. **13**, 972 (2022).
[21] T. F. Gallagher, *Rydberg Atoms* (Cambridge University Press, Cambridge, England, 1994).
[22] See Supplemental Material at http://link.aps.org/supplemental/10.1103/PhysRevLett.131.023201 for description of the experimental apparatus and timing sequence, a theoretical background, and an explanation of the numerical simulation. It includes Ref. [21] as well as Refs. [23–26].
[23] S. E. Anderson, K. C. Younge, and G. Raithel, Phys. Rev. Lett. **107**, 263001 (2011).
[24] A. Yariv and P. Yeh, *Optical Waves in Crystals* (Wiley, New York, 1984), Vol. 5.
[25] K. Dieckmann, R. J. C. Spreeuw, M. Weidemüller, and J. T. M. Walraven, Phys. Rev. A **58**, 3891 (1998).
[26] J. Dalibard and C. Cohen-Tannoudji, J. Opt. Soc. Am. B **6**, 2023 (1989).
[27] K. C. Younge, B. Knuffman, S. E. Anderson, and G. Raithel, Phys. Rev. Lett. **104**, 173001 (2010).
[28] R. Cardman and G. Raithel, Phys. Rev. A **106**, 052810 (2022).
[29] A. Ramos, K. Moore, and G. Raithel, Phys. Rev. A **96**, 032513 (2017).
[30] R. Cardman and G. Raithel, Phys. Rev. A **101**, 013434 (2020).
[31] A. Larrouy, S. Patsch, R. Richaud, J.-M. Raimond, M. Brune, C. P. Koch, and S. Gleyzes, Phys. Rev. X **10**, 021058 (2020).
[32] A. Signoles, E. K. Dietsche, A. Facon, D. Grosso, S. Haroche, J. M. Raimond, M. Brune, and S. Gleyzes, Phys. Rev. Lett. **118**, 253603 (2017).
[33] C. Feng, H. Manetsch, V. G. Rousseau, K. R. A. Hazzard, and R. Scalettar, Phys. Rev. A **105**, 063320 (2022).